

An Extended and Fragmented Alfvén Zone in the Young Solar Wind

Rohit Chhiber^{1,2*}, William H. Matthaeus¹, Arcadi V. Usmanov^{1,2}, Riddhi Bandyopadhyay³,
and Melvyn L. Goldstein⁴

¹*Department of Physics and Astronomy, University of Delaware, Newark, DE 19716, USA*

²*Heliophysics Science Division, NASA Goddard Space Flight Center, Greenbelt, MD 20771, USA*

³*Department of Astrophysical Sciences, Princeton University, Princeton, NJ 08544, USA*

⁴*University of Maryland Baltimore County, Baltimore, MD 21250, USA*

Accepted XXX. Received YYY; in original form ZZZ

ABSTRACT

Motivated by theoretical, numerical, and observational evidence, we explore the possibility that the critical transition between sub-Alfvénic flow and super-Alfvénic flow in the solar atmosphere takes place in fragmented and disconnected subvolumes within a general Alfvén critical zone. The initial observations of sub-Alfvénic periods by Parker Solar Probe near 16 R_{\odot} do not yet provide sufficient evidence to distinguish this possibility from that of a folded surface that separates simply-connected regions. Subsequent orbits may well enable such a distinction, but here we use a global magnetohydrodynamic model of the solar wind, coupled to a turbulence transport model, to generate possible realizations of such an Alfvén critical zone. Understanding this transition will inform theories of coronal heating, solar wind origin, solar angular momentum loss, and related physical processes in stellar winds beyond the Sun.

Key words: Sun: corona – solar wind – turbulence

1 INTRODUCTION

Based on known variations of magnetic field, density, and solar wind flow speed, there has long been an expectation of a transition between lower coronal sub-Alfvénic wind and super-Alfvénic solar wind (Weber & Davis 1967). In particular, given a solar wind speed V_{sw} and an Alfvén speed V_A , one expects that a sub-Alfvénic state $V_{\text{sw}} < V_A$ exists close to the sun, while a super-Alfvénic state $V_{\text{sw}} > V_A$ would dominate near Earth orbit. In the simplest wind models the transition occurs at an Alfvénic critical point. In three dimensions this readily generalizes to a smooth critical surface (e.g., Chhiber et al. 2019, and references within). Identification of this Alfvénic transition has been of interest for NASA’s Parker Solar Probe (PSP) mission since the planning stages (Matthaeus 2004; Fox et al. 2016). In fact, it has already been suggested (Matthaeus 2004; DeForest et al. 2018; Chhiber et al. 2019; Wexler et al. 2021) that the transition might be better described as a trans-Alfvénic *region* or *zone*, rather than a simple surface, in part based on remote sensing observations of an “extended solar wind transsonic (sic) region” (Lotova et al. 1985; Lotova 1988).

Even if the corona formally refers to the entirety of the solar atmosphere, there is some utility in drawing the distinction between the magnetically dominated sub-Alfvénic region as the pure corona, and the extended super-Alfvénic flow-dominated wind that permeates interplanetary space. Indeed, the crucial processes that heat the corona and accelerate the wind originate in the magnetically dominated region, thus providing a fundamental physics motivation for

the PSP mission (Fox et al. 2016). Recently, on its eighth perihelion, at a distance of about 19 R_{\odot} , PSP passed into sub-Alfvénic plasma for extended periods for the first time (Kasper et al. 2021). This has enabled the first glimpse of the magnetically dominated coronal plasma using *in situ* observations. The leading order expectations of distinctive features of coronal plasma and electromagnetic fields thus far appear to be intact (Kasper et al. 2021; Bandyopadhyay et al. 2022). In the present paper we explore how subsequent passages through this sub-Alfvénic coronal plasma might look in subsequent PSP orbits if, indeed, the trans-Alfvénic boundary is a zone rather than a well-defined surface.

The first passages of PSP into the sub-Alfvénic region have comprised several time periods, the longest of which is a few hours (Kasper et al. 2021). Further observations in more persistent sub-Alfvénic wind will be required for confirmation of these early measurements. What remains unclear is the topological nature of the trans-Alfvénic zone. Single-point observations such as those made by PSP do not readily distinguish between a folded but smooth Alfvén surface, a highly corrugated surface, or an even more complicated patchy, disconnected, or even fractal surface. Here we will develop a hybrid model – part global magnetohydrodynamic (MHD) and part synthetic and empirically justified, to visualize what an extended, fragmented Alfvén zone may appear like. Understanding this possibility in some detail may help to identify the morphology of the Alfvén transition based on subsequent PSP orbits.

The Alfvén surface departs from a simple radial critical point in even moderately realistic three-dimensional (3D) models such as source surface mappings and MHD simulations (e.g., Cohen 2015; Chhiber et al. 2019). When based on magnetogram boundary conditions, these models suggest a critical surface that exhibits asymme-

* E-mail: rohitc@udel.edu

tries in both latitude and longitude, with significant inward distortion near the heliospheric current sheet (HCS). Furthermore, recent papers based on extrapolation of in-situ measurements infer a “rugged” Alfvén surface (Wexler et al. 2021; Liu et al. 2021; Verscharen et al. 2021)

It is also expected that when fluctuations of sufficient amplitude are included, the Alfvén surface will become even more complex. Recall that the Alfvén Mach number is defined as

$$M_A(\mathbf{r}) = \frac{V_{sw}}{V_A} = \frac{V_{sw}(\mathbf{r})}{B(\mathbf{r})/\sqrt{4\pi\rho(\mathbf{r})}} \quad (1)$$

where V_{sw} , the magnetic field strength B , and the mass density ρ are all functions of position. Now suppose that the total speed, magnetic field, and density contain fluctuating components, which may be indicated as $V_{sw} = \langle V_{sw} \rangle + V'_{sw}$, $\mathbf{B} = \langle \mathbf{B} \rangle + \mathbf{B}'$ and $\rho = \langle \rho \rangle + \rho'$, where the $\langle \dots \rangle$ indicates the mean value and the prime indicates a fluctuating component that averages to zero over a few correlation scales. It is clear that when such fluctuations are present, there will be corresponding fluctuations of the Alfvén Mach number.

There are, in fact, a variety of reasons to expect that fluctuation amplitudes increase moving with the solar wind toward the Alfvén transition. Not only are there signatures of their presence in lower solar atmospheric observations (Tomczyk et al. 2007; Mathioudakis et al. 2013), but this is also expected even on the basis of WKB theory (Hollweg 1973; Velli 1993). Turbulence transport theory, containing a generalization of WKB theory, predicts an increase in fluctuation amplitude in the expanding coronal plasma, peaking near the Alfvén zone (Verdini et al. 2010). When combined self-consistently with a large-scale global solar wind MHD model (Usmanov et al. 2011, 2012, 2014, 2018), the transport theory predicts a strong maximum of fluctuation amplitude near the Alfvén critical zone (Chhiber et al. 2019). Such results can also be reproduced by an expanding box model (Squire et al. 2020) that contains physics similar to that of the turbulence transport models (see also Zank et al. 2021).

Interestingly, there have also been suggestions of a strong turbulence region near 10–30 R_\odot based on remote-sensing observations (Lotova et al. 1985; Lotova 1988; Lotova et al. 1997). Additional evidence of large fluctuations, in this case in velocity, is provided by highly sensitive chronograph observations (DeForest et al. 2018). In the latter case remote sensing indicates the presence of radially flowing electron density blobs moving outward along stream tubes with differential speeds of approximately 200 km s^{−1} along neighbouring stream tubes.

Given these diverse expectations as to the amplitudes reached by fluctuations near the Alfvén critical zone, it is understandable, in accord with Equation 1, that the Alfvén Mach number itself will fluctuate along a stream tube. Furthermore, if fluctuation amplitudes peak near the Alfvén zone, fluctuations of the Alfvén Mach number itself will peak in that region. Based on this reasoning, the critical Alfvén “surface” should be neither smooth nor a simply folded surface that each streamline passes through only once. Here we explore the possibility that there are regions or subvolumes of plasma that exist in a sub-Alfvénic state intermixed with subvolumes of super-Alfvénic flow. Thus, along flow tubes of solar wind one would repeatedly encounter subregions of sub/super-Alfvénic solar wind flows. Accordingly, the present paper is devoted to realizations of the Alfvén critical zone that include the effects of self-consistently computed fluctuations. In this way we can quantitatively assess features of the critical zone that may potentially contribute to our understanding of physical processes in the solar wind. We expect that the validity of this characterization of a fragmented Alfvén zone will be either corroborated or invalidated in future PSP orbits, as well as in anticipated

observations from next-generation remote imaging missions such as PUNCH (DeForest et al. 2019).

In outline, we briefly describe the solar wind model employed in this study in Section 2. Results are presented in Section 3, which includes a comparison of model output with PSP observations. We conclude with a discussion in Section 4.

2 SOLAR WIND MODEL WITH TURBULENCE TRANSPORT

Realistic and accurate MHD coronal simulations that resolve all scales from the large features at the solar surface to the dissipation range of solar wind turbulence are excessively demanding computationally and are at present intractable (e.g., Miesch et al. 2015). Direct simulations of turbulence effects on the Alfvén critical zone are included in this class. Therefore, to proceed we adopt an approach based on Reynolds averaging (e.g., McComb 1990) that provides explicit treatment of large scales and a self-consistent statistical treatment of the turbulence. We then generate realizations of turbulence that, when combined with the large-scale solutions, produce a picture of a turbulence-modified Alfvén zone.

A two-fluid magnetohydrodynamics (MHD) model (Usmanov et al. 2018; Gombosi et al. 2018) reasonably describes the large-scale features of the solar wind when the internal energy is separated into electron and proton fluid ingredients (Cranmer et al. 2009). The dynamics of these large-scale features is determined to a significant degree, but not completely, by boundary conditions, so that information flow is mainly along characteristics. Features separated in angle by more than a few tens of degrees do not communicate well (see, e.g., Matthaeus & Goldstein 1986). At smaller scales the system is subject to local turbulence interactions, which, although formally deterministic, are conveniently approximated by a statistical treatment, such as Reynolds averaging.

The two-fluid MHD global coronal and model that we employ is briefly summarized here, and is described in detail in Usmanov et al. (2014, 2018). The Reynolds-averaging approach is based on the decomposition of physical fields, e.g., $\tilde{\mathbf{a}}$ into a mean and a fluctuating component: $\tilde{\mathbf{a}} = \mathbf{a} + \mathbf{a}'$, making use of an ensemble-averaging operation where $\mathbf{a} = \langle \tilde{\mathbf{a}} \rangle$ and, by construction, $\langle \mathbf{a}' \rangle = 0$. Application of this decomposition to the primitive compressible MHD equations, along with a series of approximations appropriate to the solar wind, leads to a set of mean-flow equations that are coupled to the small-scale fluctuations via another set of equations for statistical descriptors of the unresolved turbulence.

To derive the mean-flow equations, the velocity and magnetic fields are Reynolds decomposed: $\tilde{\mathbf{V}} = \mathbf{V} + \mathbf{v}'$ and $\tilde{\mathbf{B}} = \mathbf{B} + \mathbf{B}'$, and then substituted into the momentum and induction equations in the frame of reference corotating with the Sun. The ensemble averaging operator $\langle \dots \rangle$ is then applied to these two equations (Usmanov et al. 2014, 2018). The resulting mean-flow model consists of a single momentum equation and separate ion and electron temperature equations, in addition to an induction equation. Density fluctuations are neglected, and pressure fluctuations are only those required to maintain incompressibility (Zank & Matthaeus 1992). The Reynolds-averaging procedure introduces additional terms in the mean flow equations, representing the influence of turbulence on the mean (average) dynamics. These terms involve the Reynolds stress tensor $\mathcal{R} = \langle \rho \mathbf{v}' \mathbf{v}' - \mathbf{B}' \mathbf{B}' / 4\pi \rangle$, the mean turbulent electric field $\boldsymbol{\varepsilon}_m = \langle \mathbf{v}' \times \mathbf{B}' \rangle (4\pi\rho)^{-1/2}$, the fluctuating magnetic pressure $\langle B'^2 \rangle / 8\pi$, and the turbulent heating, or “heat function” $Q_T(\mathbf{r})$, which is apportioned between protons and electrons. Here the mass density

$\rho = m_p N_S$ is defined in terms of the proton mass m_p and number density N_S . The pressure equations employ the natural ideal gas value of $5/3$ for the adiabatic index. The pressure equations also include weak proton-electron collisional friction terms involving a classical Spitzer collision time scale (Spitzer 1965; Hartle & Sturrock 1968) to model the energy exchange between the protons and electrons (see Breech et al. 2009). Electron heat flux below $5 - 10 R_\odot$ is approximated by the classical collision-dominated model of Spitzer & Härm (1953) (see also Chhiber et al. 2016), while above $5 - 10 R_\odot$ we adopt Hollweg’s “collisionless” conduction model (Hollweg 1974, 1976). We neglect proton heat flux. See Usmanov et al. (2018) for more details.

Transport equations for the fluctuations, assumed to be at relatively small scales, are obtained by subtracting the mean-field equations from the full MHD equations and averaging the difference (see Usmanov et al. 2014). This yields equations (Breech et al. 2008; Usmanov et al. 2014, 2018) for the three chosen statistical descriptors of turbulence, namely $Z^2 = \langle v'^2 + b'^2 \rangle$, i.e., twice the fluctuation energy per unit mass, where $\mathbf{b}' = \mathbf{B}'(4\pi\rho)^{-1/2}$; the normalized cross helicity, or normalized cross-correlation between velocity and magnetic field fluctuations $\sigma_c = 2\langle \mathbf{v}' \cdot \mathbf{b}' \rangle / Z^2$; and λ , a correlation length perpendicular to the mean magnetic field. Note that the assumption of a single correlation scale (cf. Zank et al. 2018) implies structural similarity of autocorrelation functions of the turbulent fields; this assumption was found to be reasonably valid for PSP observations (Chhiber et al. 2021c). Other parameters include the normalized energy difference, which we treat as a constant parameter ($= -1/3$) derived from observations (cf. Zank et al. 2018), and the Kármán-Taylor constants (see Matthaeus et al. 1996; Smith et al. 2001; Breech et al. 2008). Note that the fluctuation energy loss due to our assumption of von Kármán decay (de Kármán & Howarth 1938; Hossain et al. 1995; Wan et al. 2012; Wu et al. 2013; Bandyopadhyay et al. 2018) is balanced in a quasi-steady state by internal energy supply in the pressure equations. The Reynolds stress is simplified by assuming that the turbulence is transverse to the mean field and axisymmetric about it (Oughton et al. 2015), so that we obtain $\mathcal{R}/\rho = K_R(\mathbf{I} - \hat{\mathbf{B}}\hat{\mathbf{B}})$, where $K_R = \langle v'^2 - b'^2 \rangle / 2 = \sigma_D Z^2 / 2$ is the residual energy, and $\hat{\mathbf{B}}$ is a unit vector in the direction of \mathbf{B} . The turbulent electric field is neglected here. For further details see Usmanov et al. (2018).

We solve the Reynolds-averaged mean-flow equations concurrently with the turbulence transport equations in the spherical shell between the base of the solar corona (just above the transition region) and the heliocentric distance of 5 AU. The computational domain is split into two regions: the inner (coronal) region of $1 - 30 R_\odot$ and the outer (solar wind) region from $30 R_\odot - 5$ AU. The relaxation method, i.e., the integration of time-dependent equations in time until a steady state is achieved, is used in both regions. The simulations have a resolution of $702 \times 120 \times 240$ grid points along $r \times \theta \times \phi$ coordinates. The computational grid has logarithmic spacing along the heliocentric radial (r) direction, with the grid spacing becoming larger as r increases. The latitudinal (θ) and longitudinal (ϕ) grids have equidistant spacing, with a resolution of 1.5° each. In terms of physical scales, the grid spacing corresponds to several correlation lengths of magnetic fluctuations (e.g., Ruiz et al. 2014), thus providing strong motivation for the statistical model we employ for unresolved, sub-gridscale turbulence in the present study.

The model is well-tested and has been shown to yield good agreement with a variety of observations (Breech et al. 2008; Usmanov et al. 2011, 2012, 2014; Chhiber et al. 2017; Usmanov et al. 2018; Chhiber et al. 2018, 2019; Bandyopadhyay et al. 2020; Ruffolo et al. 2020; Chhiber et al. 2021c).

3 RESULTS

We now summarize the procedure employed to obtain the results below:

- (i) Initialize the global heliospheric code (Usmanov et al. 2018) with magnetogram-based boundary conditions appropriate for a specified PSP solar encounter, or a selected tilted magnetic dipole boundary condition;
- (ii) Obtain Reynolds-averaged large-scale fields and statistical turbulence parameters from the model computation;
- (iii) Employ self consistently determined turbulence parameters from the model to synthesize a plausible realization of the local turbulence fields;
- (iv) Combine mean fields and synthesized fluctuations to examine transitions between super-Alfvénic and sub-Alfvénic conditions in the trans-Alfvénic zone.

3.1 Model Runs

For the present study we performed three runs: Run I is based on a source magnetic dipole tilted by 10° relative to the solar rotation axis, toward 330° longitude in Heliographic Coordinates (HGC; Fränz & Harper 2002); Run II is based on a Wilcox Solar Observatory (WSO) magnetogram for Carrington Rotation 2215, corresponding to PSP’s first solar encounter; Run III is based on an ADAPT map with central meridian time 2021 April 29 at 12:00 UTC, corresponding to PSP’s eighth solar encounter (when the spacecraft first sampled sub-Alfvénic wind). The synoptic magnetograms from WSO have 5° resolution in heliolongitude and 30 points equidistantly distributed over the sine of heliolatitude. The ADAPT maps, which are based on the GONG magnetogram (Arge et al. 2010), have a 1° -resolution both in heliolatitude and heliolongitude. The WSO and ADAPT magnetograms are scaled by a factor of 8 and 2, respectively¹, and smoothed using a spherical harmonic expansion up to 9^{th} and 15^{th} order, respectively. Input parameters specified uniformly at the coronal base include the driving amplitude of Alfvén waves (30 km s^{-1}), and the correlation scale of turbulence (10, 500 km). In the initial state, the density and temperature are also prescribed uniformly ($8 \times 10^7 \text{ particles cm}^{-3}$ and $1.8 \times 10^6 \text{ K}$, respectively), but they can change in the course of relaxation to a steady state. The cross helicity in the initial state is set as $\sigma_c = -\sigma_{c0} B_r / B_r^{\text{max}}$, where $\sigma_{c0} = 0.8$, B_r is the radial magnetic field, and B_r^{max} is the maximum absolute value of B_r on the inner boundary. The input parameters also include the fraction of turbulent energy absorbed by protons $f_p = 0.6$, the normalized energy difference $\sigma_D = -1/3$, and Kármán-Taylor constants $\alpha = 2\beta = 0.128$. Further details on the numerical approach and initial and boundary conditions may be found in Usmanov et al. (2018), who also examined the effects of varying these parameters on the model results.

3.2 Statistical Boundaries of the Alfvén Zone

Once the boundary condition is selected and the model parameters set, steps (i) and (ii) above are straightforward. Results of this type have been used to trace critical surfaces for comparison with remote imaging (Chhiber et al. 2018, 2019), to make predictions for PSP

¹ This scaling is required to obtain agreement between model results and spacecraft observations near Earth (see Riley et al. 2014). The choice of scaling factor and its effects on model output are discussed in detail by Usmanov et al. (2018).

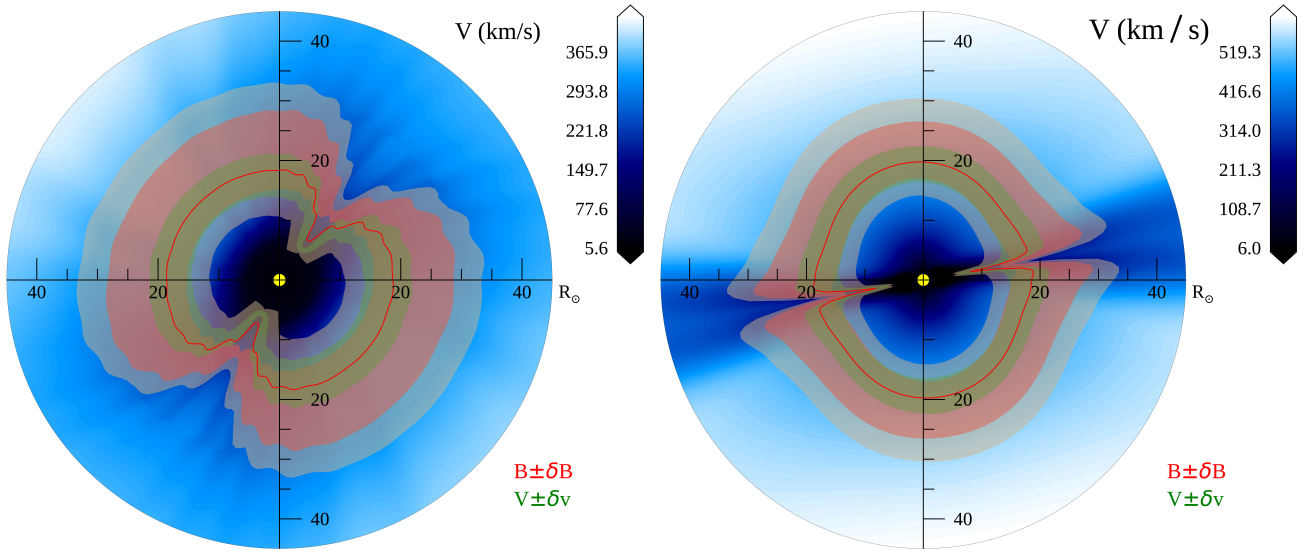


Figure 1. Solar wind speed and the effect of fluctuations on the Alfvén zone. Left and right panels show the solar equatorial plane (r - ϕ plane at 0° latitude) and a meridional plane (r - θ plane at 155° longitude), respectively, for the 10° dipole-based Run I. Helioradii ranging from 1 to $45 R_\odot$ are shown in both panels. Red curve shows the Alfvén surface computed using the mean velocity and magnetic fields. Red-shaded region shows the range of distances at which the trans-Alfvénic transition can occur when magnetic fluctuations are accounted for (see text). Green-shaded region shows this trans-Alfvénic zone when velocity fluctuations, but not magnetic fluctuations are included. The widest, beige-shaded region shows this zone when both magnetic and velocity fluctuations are included.

crossings of critical surfaces (Chhiber et al. 2019), and for comparison of model results with mean-field and turbulence measurements along the PSP trajectory for orbits 1 through 5 (Chhiber et al. 2021c). Determination of a consistent realization of the turbulence in step (iii) is a novel procedure that we describe here in order to estimate turbulence effects on the topography of the trans-Alfvénic critical region.

To extract rms amplitudes for magnetic and velocity fluctuations from the Z^2 variable computed in the turbulence transport model, we assume an Alfvén ratio $r_A \equiv \langle v'^2 \rangle / \langle B'^2 \rangle = 0.5$, following observations from PSP and near-Earth spacecraft (Tu & Marsch 1995; Chen et al. 2020; Parashar et al. 2020); this is also consistent with the constant energy difference $\sigma_D = (r_A - 1)/(r_A + 1) = -1/3$ assumed in our model (cf. Zank et al. 2018). Then we obtain 3D distributions of rms velocity and magnetic fluctuation amplitudes using the expressions $\delta v \equiv \langle v'^2 \rangle^{1/2} = [Z^2/(1 + 1/r_A)]^{1/2}$ and $\delta B \equiv \langle B'^2 \rangle^{1/2} = [Z^2 4\pi\rho/(1 + r_A)]^{1/2}$, respectively.

An analogous procedure is used to obtain the partitioning of fluctuation energy among the three local Cartesian components of polarization. The transport model described in Section 2 adopts the approximation that the fluctuations have purely transverse polarizations, for analytical tractability (Breech et al. 2008; Usmanov et al. 2014). However, to preserve the magnetic field’s divergenceless nature, Alfvénic-type fluctuations of finite amplitude must include three components of polarization (Barnes 1976, 1979). We adopt a simple isotropic partitioning in this initial study, noting that the Alfvén Mach number is computed using the magnitudes of the solar wind speed and magnetic field, and is therefore not very sensitive to the relative strengths of individual local Cartesian components. Then each fluctuating component δB_i has a variance $\delta B_i^2 = \delta B^2/3$, where $i \in \{r, \theta, \phi\}$. A similar procedure is used to estimate components of velocity fluctuations.

With these preparations we are now in a position to examine the effect of turbulence on the location of the Alfvén surface. We estimate upper and lower statistical bounds for the total magnetic and velocity

fields, taking into account rms fluctuations about the mean values: the upper and lower bounds for the solar wind speed are computed as $V_\pm = |V \pm \delta v| = [(V_r \pm \delta v_r)^2 + (V_\theta \pm \delta v_\theta)^2 + (V_\phi \pm \delta v_\phi)^2]^{1/2}$, and the corresponding bounds for the Alfvén speed are $V_{A\pm} = [(B_r \pm \delta B_r)^2 + (B_\theta \pm \delta B_\theta)^2 + (B_\phi \pm \delta B_\phi)^2]^{1/2}/(4\pi\rho)^{1/2}$.

Based on these procedures, Figure 1 illustrates features of the Alfvén critical zone represented in the solar equatorial plane (left panel) and a meridional plane (right panel). The background shows a colour map of the solar wind speed, exhibiting familiar features of acceleration and fast/slow wind streams (McComas et al. 2003). The trans-Alfvénic boundary is computed in four different ways: The red curve shows the Alfvén surface computed in the conventional way (e.g., Chhiber et al. 2019), as the set of points where the mean solar wind speed V first becomes larger than the Alfvén speed computed from the mean magnetic field: $V_A = B/(4\pi\rho)^{1/2}$. Away from the HCS this “mean” Alfvén surface is located at $\sim 18 R_\odot$. The red-shaded Alfvén zone is bound by outer and inner envelopes defined by the set of points where the condition $V > V_{A\pm}$ is first attained approaching from larger radial distances (outer envelope), or from smaller radial distances (inner envelope); only the effect of magnetic fluctuations is taken into account. Note that the mean-field Alfvén surface marked by the red curve dips below the red-shaded zone at the HCS, where the mean magnetic field vanishes, leading to a small mean Alfvén speed. The green-shaded zone is obtained in a similar way, by considering the condition $V_\pm > V_A$, i.e., accounting for velocity fluctuations only. Finally, the beige-shaded zone accounts for both magnetic and velocity fluctuations by using the condition $V_\pm > V_{A,\pm}$. One may observe from this relatively crude exercise that, away from the HCS, and for this particular case, the position of the critical surface can be displaced, on average, by 5 to $10 R_\odot$ by the (approximate) influence of magnetic turbulence. Velocity fluctuations produce a relatively weaker effect (partly due to the choice of Alfvén ratio), which is also symmetric about the “mean” Alfvén surface (red curve). As expected, combining velocity and magnetic

fluctuations produces the largest variability, with the Alfvén surface shifted by as much as $15 R_{\odot}$.

3.3 Realization of a Fragmented Alfvén Zone

While the above procedure permits estimation of the *average* spatial extent of the Alfvén critical zone, we can provide additional detail, again in an approximate but consistent sense, by adopting a specific field of turbulence that is based on the turbulence model incorporated in the Reynolds-averaged MHD simulations. To examine the effect of an explicit realization of turbulence on the Alfvén zone, we generate synthetic random fluctuations that are constrained by the rms turbulence amplitudes described in the previous section.² These fluctuations, inserted into Equation 1, enable us to examine a plausible spatial dependence of the Alfvén Mach number while including the effect of turbulence.

For this first study, we examine the effect of magnetic fluctuations, although velocity and density fluctuations can also, in principle, be incorporated in an analogous way. At each point on the simulation grid, $\{r, \theta, \phi\}$ components of a random magnetic fluctuation vector are generated: each component $(B'_r, B'_\theta, B'_\phi)$ is a random number obtained from a Gaussian distribution with standard deviation equal to the respective rms magnetic fluctuation component given by the model at that point (see Section 3.2).³ The total magnetic field magnitude is then $\tilde{B} = [(B_r + B'_r)^2 + (B_\theta + B'_\theta)^2 + (B_\phi + B'_\phi)^2]^{1/2}$, and thus we obtain a 3D distribution of Alfvén speed that includes an explicit realization of magnetic fluctuations: $\tilde{V}_A = \tilde{B}/\sqrt{4\pi\rho}$. In the following, \tilde{V}_A is compared with the mean solar wind speed V to compute the local Alfvén Mach number at a simulation grid point.

Figure 2 depicts the values of $M_A = V/\tilde{V}_A$ in a meridional plane for a 10° -tilt dipole simulation (Run I). The image is nearly rotationally symmetric except for the indentation feature associated with the HCS. With the exception of that region, the many transitions from low Alfvén Mach number (shades of green/black) to high Alfvén Mach number (shades of red/orange) occur mainly in a band that extends from around $12 R_{\odot}$ to about $25 R_{\odot}$. The range of this band is comparable to what is seen in the red-shaded region of Figure 1. Within this band we observe patches of plasma with $M_A > 1$ interspersed with sub-Alfvénic patches.

Figure 3 shows a further analysis of the tilted dipole run, including both an equatorial plane (left) and a meridional plane (right). Within each, the super-Alfvénic (teal) and sub-Alfvénic (beige) regions are distinguished by colour, where the realization of magnetic turbulence is included in the determination as in Figure 2. The solid black line (near $20 R_{\odot}$) indicates the position of the simple critical surface that is obtained when the turbulence is not taken into account (i.e., only the large-scale mean fields are included in Equation 1), and corresponds exactly to the red curve in Figure 1. Note that if no turbulence were present the interior of the black contour would be entirely beige, and the exterior, teal. It is apparent that the effect of the turbulence is to cause a disjoint or fragmented transition between super- and sub-Alfvénic regions. Moving inward from large distances, one is likely to encounter sporadic patches of sub-Alfvénic flow in regions

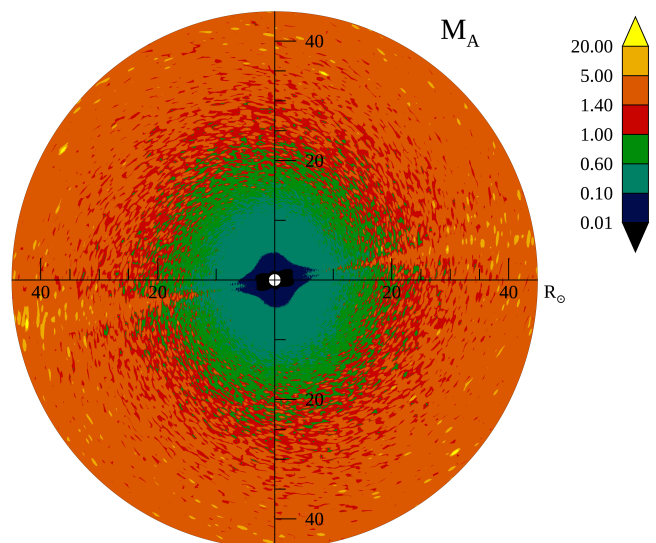


Figure 2. Alfvén Mach number in a meridional plane at 155° longitude, from Run I (10° -tilt dipole). Helioradii ranging from 1 to $45 R_{\odot}$ are shown. The Alfvén speed is computed from a magnetic field that includes an explicit realization of fluctuations, constrained by the turbulence transport model (see text).

that are dominantly super-Alfvénic.⁴ Below the black contour the dominance of the sub-Alfvénic patches increases and the patchiness eventually gives way to pure sub-Alfvénic wind. The radius within which the flow is purely sub-Alfvénic is indicated by the inner red contour. For this run that distance is irregular, but roughly near $12 R_{\odot}$. Similarly, moving inward along any radial spoke, the largest distance at which a sub-Alfvénic patch or blob is encountered, is indicated by the outer red contour. The two dashed black curves mark the “average” trans-Alfvénic region obtained by adding/subtracting the local rms magnetic fluctuation amplitude to the mean magnetic field, and correspond exactly to the boundaries of the red-shaded zone in Figure 1.

Very similar properties are found when the above analyses are carried out using a simulation run initialized with boundary conditions derived from an appropriate magnetogram (see Section 3.1). This approach affords a greater degree of realism and a rough contextual connection to conditions seen in PSP observations. Figure 4 shows results of such an analysis based on Run II, in the same format as the previous figure. In this case the Alfvén Mach number in the equatorial plane displays a somewhat more irregular pattern in comparison to the tilted dipole run in Figure 3. This irregularity is manifest in both the overall morphology including the turbulence realization, and is also seen in the black contour evaluated from the mean fields alone. The inner and outer contours (in red) demarcating the domain of the Alfvén critical zone are also rather irregular in this case, and are found closer to the sun than in the dipole case. This is partially due to the rapid radial decay of the higher-order multipole magnetic fields that are implied by a complex magnetogram boundary condition (Réville et al. 2015; Chhiber et al. 2019), and also due to the closer position

² A similar approach was used in Chhiber et al. (2021c) for a comparison of synthetic magnetic fluctuations with PSP observations.

³ We use the IDL function `randumu`, which is based on the Mersenne Twister algorithm for generating pseudo-random numbers (Matsumoto & Nishimura 1998). Note that these numbers may have positive or negative sign.

⁴ The granularity of the patches is constrained by the resolution of the simulation grid. Recall that the grid resolution is of the order of a few correlation lengths, which is consistent with our approach in which random synthetic fluctuations at neighboring vertices are uncorrelated. Grid spacings finer than a correlation scale may require a different approach.

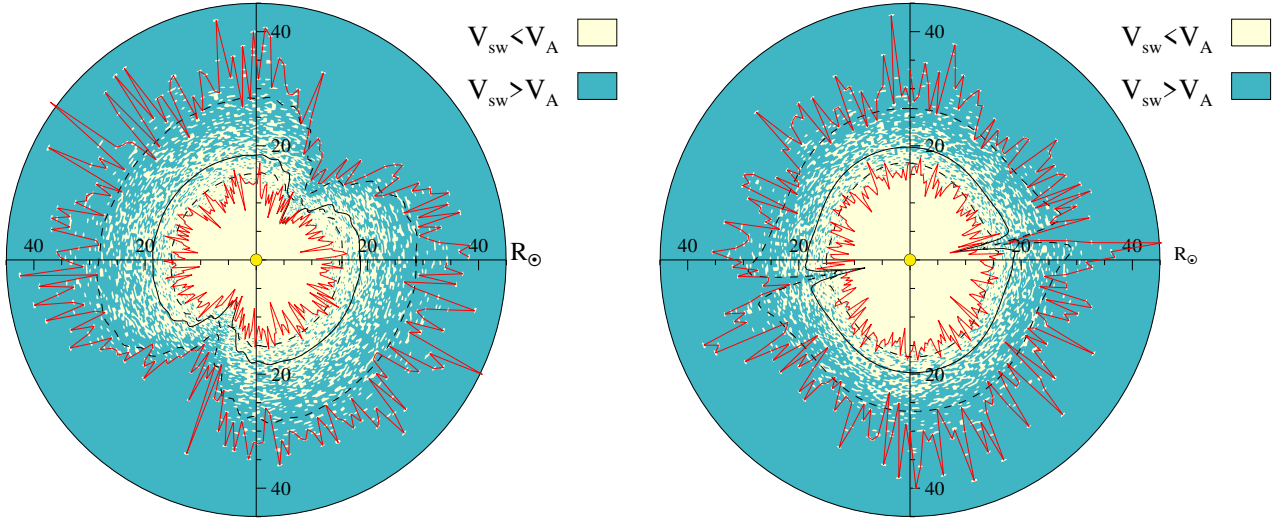


Figure 3. Sub-Alfvénic (beige) and super-Alfvénic (teal) regions are distinguished by colour, in a calculation that includes an explicit realization of magnetic turbulence (see text). Left and right panels show the solar equatorial plane and a meridional plane at 155° longitude, respectively, for a 10° -tilt dipole simulation (Run I). Helioradii ranging from 1 to $45 R_\odot$ are shown. Solid black curve shows the Alfvén surface computed from the mean fields. The two dashed black curves demarcate the “average” trans-Alfvénic region obtained by adding/subtracting the local rms magnetic fluctuation amplitude to the mean magnetic field, and correspond exactly to the boundaries of the red-shaded zone in Figure 1 (see Section 3.2). The inner red curve marks, for each θ and ϕ , the first super-Alfvénic (teal) point while moving outward along a radial spoke. Similarly, the outer red curve marks the last sub-Alfvénic (beige) point while moving outward along a radial spoke.

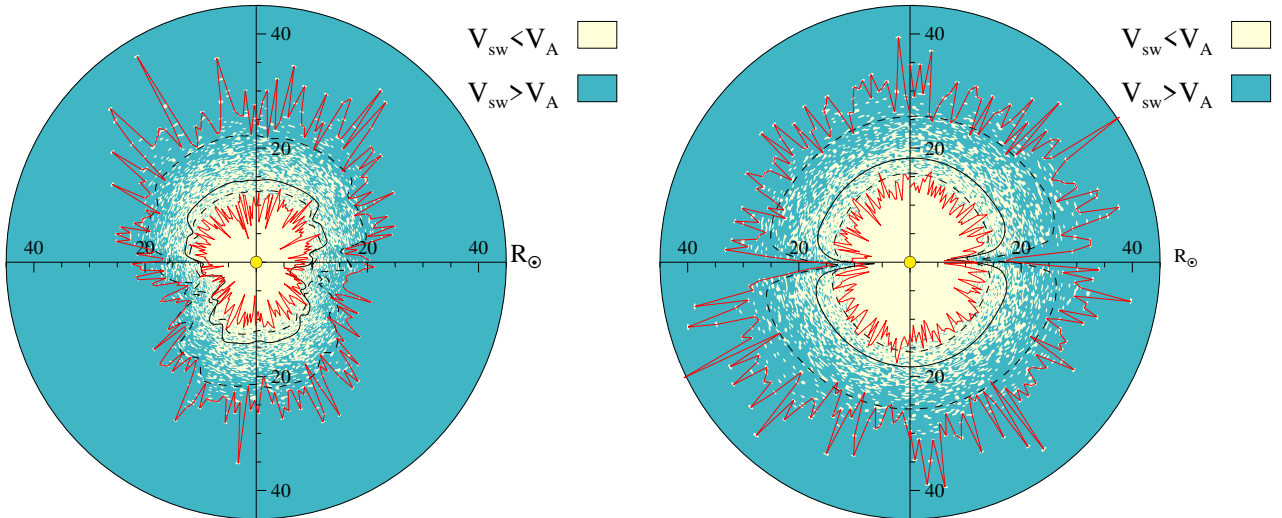


Figure 4. Left and right panels show the solar equatorial plane and a meridional plane at 155° longitude, respectively, from Run II, based on a Nov 2018 magnetogram. The description follows Figure 3.

of the HCS relative to the solar equatorial plane in the magnetogram. The latter point is made clear in the right panel of Figure 4, which illustrates the trans-Alfvénic region in a meridional plane using the same magnetogram run.

The panels of Figure 4 also confirm the main finding of this study – that the transitions between sub-Alfvénic and super-Alfvénic flows occur initially in patches, which become more densely packed moving across the Alfvén transition zone. This gradual transition is readily quantified by computing the fraction of points in the simulation that are sub-Alfvénic, as a function of radial distance. For clarity, the results are averaged over solar longitude, and subject to a simple sorting by latitude. Figure 5 shows the result of such calculations,

for the tilted-dipole simulation discussed above (Run I). This is done for the full model including turbulence at high latitudes $|\theta| > 30^\circ$ and at low latitudes $|\theta| < 30^\circ$, and for a simple model of a single “wrinkled”, or corrugated Alfvén surface (see caption).⁵ The rela-

⁵ The latter model is based on a conception of fluctuations that are advected by the mean flow and do not vary in r , therefore implying a single transition from sub-Alfvénic to super-Alfvénic flow along each radial spoke. Motivated by recent coronagraph observations (DeForest et al. 2018) that indicate velocity fluctuations of the order of 100 km s^{-1} in the region $5\text{--}15 R_\odot$, we generate a realization of random velocity fluctuations for each θ and ϕ on the simulation grid, drawn from a Gaussian distribution with a standard deviation of 100

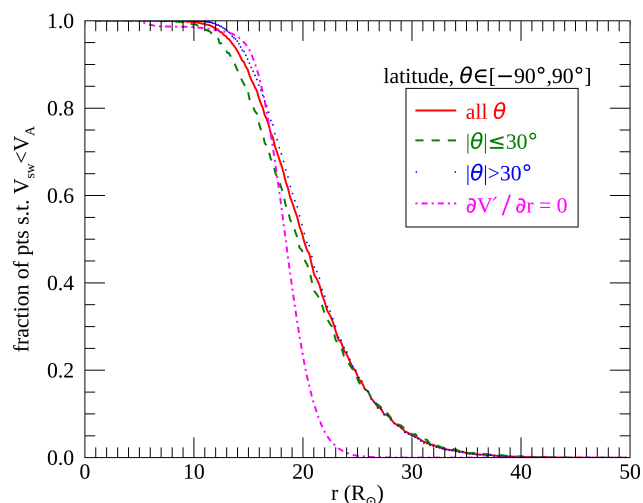


Figure 5. Filling fraction of sub-Alfvénic plasma, based on Run I. Fractions for each r are computed across all longitudes and indicated latitudes. The solid red, dashed green, and dotted blue curves are based on the realization of magnetic fluctuations described in Figure 3. The dash-dotted magenta curve is based on a realization of random velocity fluctuations (ignoring magnetic fluctuations) that do not vary in r and therefore produce a single “wrinkled”, or corrugated Alfvén surface (see text). Fractions at each r for this curve are computed for all longitudes and latitudes.

tively gradual transition in the patchy Alfvén zone case may provide a basis for distinguishing it from the single folded-surface case (dash-dotted curve) which transitions more abruptly. We cannot rule out that varying the procedure used to model the latter case may modify the comparison in Figure 5.

3.4 Comparison with PSP Observations

The fields computed by the Reynolds-averaged simulations have been recently compared with PSP observations in some detail (Chhiber et al. 2021c). In that case a number of parameters were found to agree well with PSP observations along its orbit, and in some cases, the envelope of variations implied by the computed turbulence parameters demonstrated potential consistency between simulation and observation. For one case in that paper, a realization of switchbacks was compared with PSP magnetic field data to demonstrate both successes and shortcomings of this approach. Here we take this approach to comparison of PSP with simulation a step further and compare samples of the Alfvén Mach number time series from PSP data with a synthetic time series derived from a realization of the full 3D fields that determine the Mach number.

Using the simulations driven by magnetograms corresponding to PSP’s first and eighth encounters (Runs II and III, respectively), we construct the spatial distribution of mean fields and turbulence parameters, and then, a realization of the turbulence, which is superposed on the computed mean fields, as described in Section 3.3. The Alfvén Mach number is computed throughout the simulation domains, and then (trilinearly) interpolated to the PSP trajectory at

km s^{-1} . The total solar wind speed (including fluctuations) is computed in an analogous way to the procedure described in Section 3.3 for the magnetic field. This speed is then compared with the Alfvén speed computed from the mean fields to produce the dash-dotted magenta curve in Figure 5.

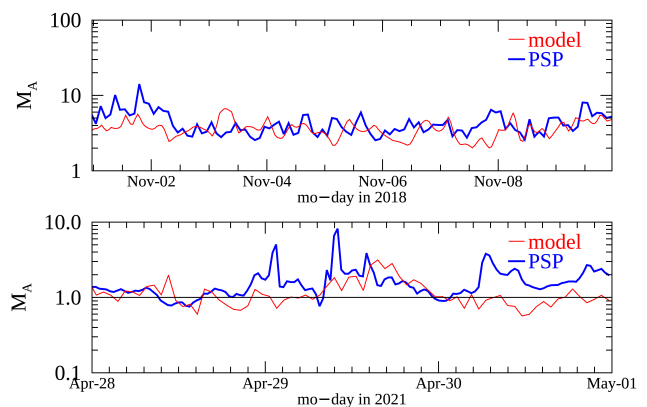


Figure 6. Alfvén Mach number along simulated PSP trajectory (thinner red curve), compared with PSP observations (thicker blue curve). Data are plotted at 1-hour cadence. Top (bottom) panel is based on Run II (Run III) and PSP observations from the first (eighth) solar encounter. The model curves include the effect of synthetic magnetic fluctuations, as described in Section 3.3.

1-hour cadence. The observations are smoothed to 1-hour cadence for comparison with the model. Two samples of results of this type are shown in Figure 6.

The top panel shows the Alfvén mach number M_A for an approximately eight day period at the beginning of November 2018, near the first perihelion at about $36 R_\odot$ (for details of PSP-data processing see Chhiber et al. 2021c). The model result, including synthetic fluctuations, qualitatively matches the PSP data, in terms of general trend and in terms of the magnitude of the fluctuations. Of course, the comparison of actual waveform to synthetic waveform should not be taken seriously, since only the local variances are physically meaningful.

The bottom panel of Figure 6 shows another comparison of M_A of the same type, in this case near the eighth perihelion at $\sim 16 R_\odot$. For details on the processing of PSP measurements see Bandyopadhyay et al. (2022). It is apparent that the Alfvén Mach number dips below unity several times in this period; these are the first sub-Alfvénic periods observed by PSP, as reported by Kasper et al. (2021) and further analyzed by Bandyopadhyay et al. (2022). The agreement is again rather good considering that the phases of the fluctuations are random, and only the local variances are meaningful. For example, the more extended period of sub-Alfvénic flow in the second half of April 28 is approximately accounted for by model, but the sub-Alfvénic period seen only in the simulation between April 30 and May 1 is apparently an artifact.

4 DISCUSSION

A number of current and recent observations (Liu et al. 2021; Wexler et al. 2021) suggest that the Alfvén critical surface is not a simple smooth symmetric surface. Remote sensing observations (Lotova et al. 1985; Lotova 1988) indicate a range of distances in which a critical transition might occur. Recent detections of sub-Alfvénic regions near PSP perihelia also indicate a possible range of distances associated with the transition (Kasper et al. 2021). Predictions of ranges of distances also have been reported based on extrapolation of in-situ measurements (Goelzer et al. 2014; Kasper & Klein 2019; Wexler et al. 2021). In addition to a distorted or folded simple surface, more complex possibilities exist that amount to a state in which

the transition occurs over a significant range of distances – in an Alfvén transition zone or region (Lotova et al. 1985; Matthaeus 2004; DeForest et al. 2018; Chhiber et al. 2019). Based on the expected large amplitude of turbulent fluctuations near the critical region, we postulate that the transition occurs in fragmented patches rather than in a folded or distorted simply-connected surface. Here we provide empirical support for this possibility based on a Reynolds-averaged model that includes, crucially, turbulence transport (Usmanov et al. 2018).

One feature we discussed in some detail is the extent of the Alfvén critical region, bounding it with inner and outer surfaces defined by the first and last trans-Alfvénic blob along each radial “spoke”. Between these lies the simple Alfvén surface that would be present if no turbulent fluctuations were present and the Alfvén mach number is calculated in terms of only the computed mean fields. Arguably, any of these three contours (inner, mean field, or outer) could be used to define an “Alfvén surface”, depending on the intent of the adopted definition. But it is equally clear that for this realization there is no simply-connected critical surface in the usual sense (Matthaeus 2004). Instead, the above constructs provide a demarcation of what might properly be called a trans-Alfvénic zone.

A salient feature of this empirical demonstration of a fragmented Alfvén critical zone is the appearance of subvolumes or blobs of sub-Alfvénic (super-Alfvénic) flow in regions that are predominantly super-Alfvénic (sub-Alfvénic). The blobs are of varying size and are visibly clumped in many locations, indicating correlations among the population. Their random character emerges as a convolution of the complex dynamics driven by the magnetogram boundary conditions, and the stochastic realization of the turbulence amplitudes (implemented here in an *ad hoc* procedure constrained by the local value of the average turbulence amplitude provided by the model). The latter property is not entirely an artifact, since the random numbers employed are drawn for each computational vertex, which are separated by somewhat more than a turbulence correlation length. Therefore the vector fields in adjacent vertices are expected to be almost uncorrelated even if the turbulence amplitudes maintain a mutual correlation, established at the photospheric boundary and maintained approximately along (many) nearby MHD characteristics.

Another feature of the trans-Alfvénic blobs is that their aggregate perimeter, or the length of their “coastline” is certain to be quite large. The question of whether the lengths of these perimeters scale, like the coastline of Britain, in a way that signifies a fractal distribution (Mandelbrot 1967) is a technical question that we defer to future study. In any case, the MHD wave characteristics in this region are expected to be extremely complex (Verdini et al. 2009), and the behaviour of waves at these apparently complex interfaces may also be an ingredient of coronal heating models worthy of additional examination. Finally, we might ask whether the irregular distribution of trans-Alfvénic patches or blobs represent a type of spatial intermittency. Referring again to the relatively large size of these patches (in the present implementation), it would seem doubtful that their distribution contributes directly to either inertial range or dissipation range intermittency (Sreenivasan & Antonia 1997; Matthaeus et al. 2015), which are generally described in terms of increments at lags much smaller than the correlation scale (e.g., Sorriso-Valvo et al. 1999; Chhiber et al. 2021b). However, the type of large-scale intermittency described by Oboukhov in his seminal 1962 paper may be relevant here: in particular, the author writes “These slow fluctuations of energy dissipation are due to change of the large-scale processes in the observation region, or ‘weather’ in a general sense.” (Oboukhov 1962). This directly motivates Oboukhov’s introduction of log-normal statistics into the formulation of turbulent intermit-

tency. Lognormal statistics are pervasive in solar wind parameters including the distributions of magnetic field strength (Burlaga & Ness 1998) and correlation scale (Ruiz et al. 2014), and is a factor underlying the possible origin of so-called $1/f$ noise in the interplanetary magnetic field (Matthaeus & Goldstein 1986). The distribution of fragmented trans-Alfvénic regions is still another possible example of large-scale intermittency due to gusty solar “weather”. Indeed there may be many interesting connections and directions for further work indicated by the current conceptual and semi-empirical study.

One can imagine reasonable modifications to the procedure used here to generate synthetic fluctuations; these include different values for the Alfvén ratio, variance polarization anisotropy, and the inclusion of velocity and density fluctuations in addition to magnetic. Nevertheless, we do not expect such changes to affect the qualitative conceptual picture we have proposed. We emphasize the novelty of our approach for generating an explicit realization of turbulent fluctuations within the context of a Reynolds-averaged global solar wind model; with further refinements this technique can find a variety of applications, such as studies of energetic particle transport (e.g., Moradi & Li 2019; Chhiber et al. 2021a).

The observational question that remains is whether the simple surface model or the extended, fragmented zone model is more realistic. Our empirical model provides predictions for future PSP observations, which might possibly be used to distinguish between “surface vs zone” pictures – our model implies greater density/frequency-of-occurrence of sub-Alfvénic patches, and longer durations as well, as PSP descends to lower perihelia. The surface picture implies longer durations of sub-Alfvénic intervals as PSP descends, instead of increasing density and frequency of such intervals; this picture also most likely is associated with sharper transitions (see Figure 5).

Later PSP orbits will provide opportunities for possible support for the present perspective. We would argue that successive orbits at lower heliocentric distances will continue to observe patches of sub-Alfvénic flow but at increasing rates and higher filling fractions at lower perihelia, until finally arriving at pure or nearly pure sub-Alfvénic flow. There is no guarantee that PSP orbits will probe deeply enough to arrive in the pure sub-Alfvénic coronal plasma. Even still, the radial trends may permit further analysis to distinguish the fragmented patchy transition that we explore here, from a simpler “wrinkled”, or corrugated surface model such as that we described above. This distinction may prove to be important in distinguishing different coronal heating models, since a fragmented transition zone may provide a kind of “pressure cooker” for enhanced heating by interaction of reflected “inward” type waves with the dominant outward propagating Alfvénic fluctuations (Matthaeus et al. 1999). Other types of simulations, such as the so-called expanding box model (Grappin et al. 1993; Squire et al. 2020), may also provide additional insights into the “surface vs zone” question. In any case, observations by any single spacecraft may not be able to recover enough 3D information to conclusively determine the topography of the Alfvénic transition zone. It is, however, hoped that sophisticated polarized imaging instruments on the PUNCH mission (DeForest et al. 2019), designed to provide high resolution 3D data, will be able to make this important determination.

ACKNOWLEDGEMENTS

This research partially supported by NASA under the Heliospheric Supporting Research program grants 80NSSC18K1210 and 80NSSC18K1648 and by the Parker Solar Probe Guest Investigator program 80NSSC21K1765, the PSP/IS \odot IS Theory and Model-

ing project (Princeton subcontract SUB0000165), and the PUNCH project under subcontract NASA/SWRI N99054DS. We thank Dr. Francesco Pucci for suggesting the designation “antarctic plot” for Figures 3 and 4. This work utilizes data produced collaboratively between AFRL/ADAPT and NSO/NISP. Computing resources supporting this work were provided by the NASA High-End Computing (HEC) Program (awards SMD-17-1580 and SMD-17-1617) through the NASA Advanced Supercomputing Division at Ames Research Center. We acknowledge the PSP mission for use of the data, which are publicly available at the [NASA Space Physics Data Facility](#).

DATA AVAILABILITY

Simulation data will be made available upon reasonable request to the corresponding author. PSP data are publicly available at the [NASA Space Physics Data Facility](#).

REFERENCES

- Arge C. N., Henney C. J., Koller J., Compeau C. R., Young S., MacKenzie D., Fay A., Harvey J. W., 2010, in Maksimovic M., Issautier K., Meyer-Vernet N., Moncuquet M., Pantellini F., eds, American Institute of Physics Conference Series Vol. 1216, Twelfth International Solar Wind Conference. pp 343–346, [doi:10.1063/1.3395870](#)
- Bandyopadhyay R., Oughton S., Wan M., Matthaeus W. H., Chhiber R., Parashar T. N., 2018, *Phys. Rev. X*, **8**, 041052
- Bandyopadhyay R., et al., 2020, *ApJS*, **246**, 48
- Bandyopadhyay R., Matthaeus W. H., McComas D. J., Chhiber R., Usmanov A. V., Others 2022, *Astrophys. J. Lett. (In Press)*, 00, 0000
- Barnes A., 1976, *J. Geophys. Res.*, **81**, 281
- Barnes A., 1979, Hydromagnetic waves and turbulence in the solar wind. National Academies Press, pp 249–319
- Breech B., Matthaeus W. H., Minnie J., Bieber J. W., Oughton S., Smith C. W., Isenberg P. A., 2008, *Journal of Geophysical Research (Space Physics)*, **113**, A08105
- Breech B., Matthaeus W. H., Cranmer S. R., Kasper J. C., Oughton S., 2009, *Journal of Geophysical Research (Space Physics)*, **114**, A09103
- Burlaga L. F., Ness N. F., 1998, *J. Geophys. Res.*, **103**, 29719
- Chen C. H. K., et al., 2020, *ApJS*, **246**, 53
- Chhiber R., Usmanov A., Matthaeus W., Goldstein M., 2016, *ApJ*, **821**, 34
- Chhiber R., Subedi P., Usmanov A. V., Matthaeus W. H., Ruffolo D., Goldstein M. L., Parashar T. N., 2017, *ApJS*, **230**, 21
- Chhiber R., Usmanov A. V., DeForest C. E., Matthaeus W. H., Parashar T. N., Goldstein M. L., 2018, *ApJ*, **856**, L39
- Chhiber R., Usmanov A. V., Matthaeus W. H., Goldstein M. L., 2019, *ApJS*, **241**, 11
- Chhiber R., et al., 2021a, *A&A*,
- Chhiber R., Matthaeus W. H., Bowen T. A., Bale S. D., 2021b, *ApJ*, **911**, L7
- Chhiber R., Usmanov A. V., Matthaeus W. H., Goldstein M. L., 2021c, *ApJ*, **923**, 89
- Cohen O., 2015, *Sol. Phys.*, **290**, 2245
- Cranmer S. R., Matthaeus W. H., Breech B. A., Kasper J. C., 2009, *ApJ*, **702**, 1604
- DeForest C. E., Howard R. A., Velli M., Viall N., Vourlidas A., 2018, *ApJ*, **862**, 18
- DeForest C. E., Gibson S. E., Beasley M., Colaninno R. C., Killough R., Kosmann W., Laurent G. T., McMullin D. R., 2019, in AGU Fall Meeting Abstracts. pp SH43B–06
- Fox N. J., et al., 2016, *Space Sci. Rev.*, **204**, 7
- Fränz M., Harper D., 2002, *Planet. Space Sci.*, **50**, 217
- Goelzer M. L., Schwadron N. A., Smith C. W., 2014, *Journal of Geophysical Research (Space Physics)*, **119**, 115
- Gombosi T. I., van der Holst B., Manchester W. B., Sokolov I. V., 2018, *Living Reviews in Solar Physics*, **15**, 4
- Grappin R., Velli M., Mangeney A., 1993, *Physical Review Letters*, **70**, 2190
- Hartle R. E., Sturrock P. A., 1968, *ApJ*, **151**, 1155
- Hollweg J. V., 1973, *J. Geophys. Res.*, **78**, 3643
- Hollweg J. V., 1974, *J. Geophys. Res.*, **79**, 3845
- Hollweg J. V., 1976, *J. Geophys. Res.*, **81**, 1649
- Hossain M., Gray P. C., Pontius Jr. D. H., Matthaeus W. H., Oughton S., 1995, *Physics of Fluids*, **7**, 2886
- Kasper J. C., Klein K. G., 2019, *ApJ*, **877**, L35
- Kasper J. C., et al., 2021, *Phys. Rev. Lett.*, **127**, 255101
- Liu Y. D., Chen C., Stevens M. L., Liu M., 2021, *ApJ*, **908**, L41
- Lotova N. A., 1988, *Sol. Phys.*, **117**, 399
- Lotova N. A., Blums D. F., Vladimirovskii K. V., 1985, *A&A*, **150**, 266
- Lotova N. A., Vladimirovskii K. V., Korelov O. A., 1997, *Sol. Phys.*, **172**, 225
- Mandelbrot B., 1967, *Science*, **156**, 636
- Mathioudakis M., Jess D. B., Erdélyi R., 2013, *Space Sci. Rev.*, **175**, 1
- Matsumoto M., Nishimura T., 1998, *ACM Trans. Model. Comput. Simul.*, **8**, 3–30
- Matthaeus W. H., 2004, arXiv e-prints, [p. arXiv:2106.08450](#)
- Matthaeus W. H., Goldstein M. L., 1986, *Physical Review Letters*, **57**, 495
- Matthaeus W. H., Zank G. P., Oughton S., 1996, *Journal of Plasma Physics*, **56**, 659
- Matthaeus W. H., Zank G. P., Oughton S., Mullan D. J., Dmitruk P., 1999, *ApJ*, **523**, L93
- Matthaeus W. H., Wan M., Servidio S., Greco A., Osman K. T., Oughton S., Dmitruk P., 2015, *Philosophical Transactions of the Royal Society of London Series A*, **373**, 20140154
- McComas D. J., Elliott H. A., Schwadron N. A., Gosling J. T., Skoug R. M., Goldstein B. E., 2003, *Geophys. Res. Lett.*, **30**, 1517
- McComb W. D., 1990, The Physics of Fluid Turbulence. Clarendon Press Oxford
- Miesch M., et al., 2015, *Space Sci. Rev.*, **194**, 97
- Moradi A., Li G., 2019, *ApJ*, **887**, 102
- Oboukhov A. M., 1962, *Journal of Fluid Mechanics*, **13**, 77
- Oughton S., Matthaeus W., Wan M., Osman K., 2015, *Phil. Trans. R. Soc. A*, **373**, 20140152
- Parashar T. N., et al., 2020, *ApJS*, **246**, 58
- Réville V., Brun A. S., Matt S. P., Strugarek A., Pinto R. F., 2015, *ApJ*, **798**, 116
- Riley P., et al., 2014, *Sol. Phys.*, **289**, 769
- Ruffolo D., et al., 2020, *ApJ*, **902**, 94
- Ruiz M. E., Dasso S., Matthaeus W. H., Weygand J. M., 2014, *Solar Physics*, **289**, 3917
- Smith C. W., Matthaeus W. H., Zank G. P., Ness N. F., Oughton S., Richardson J. D., 2001, *J. Geophys. Res.*, **106**, 8253
- Sorriso-Valvo L., Carbone V., Veltri P., Consolini G., Bruno R., 1999, *Geophys. Res. Lett.*, **26**, 1801
- Spitzer L., 1965, Physics of fully ionized gases. Interscience Publishers
- Spitzer L., Härm R., 1953, *Physical Review*, **89**, 977
- Squire J., Chandran B. D. G., Meyrand R., 2020, *ApJ*, **891**, L2
- Sreenivasan K. R., Antonia R. A., 1997, *Annual Review of Fluid Mechanics*, **29**, 435
- Tomczyk S., McIntosh S. W., Keil S. L., Judge P. G., Schad T., Seeley D. H., Edmondson J., 2007, *Science*, **317**, 1192
- Tu C.-Y., Marsch E., 1995, *Space Sci. Rev.*, **73**, 1
- Usmanov A. V., Matthaeus W. H., Breech B. A., Goldstein M. L., 2011, *ApJ*, **727**, 84
- Usmanov A. V., Goldstein M. L., Matthaeus W. H., 2012, *ApJ*, **754**, 40
- Usmanov A. V., Goldstein M. L., Matthaeus W. H., 2014, *ApJ*, **788**, 43
- Usmanov A. V., Matthaeus W. H., Goldstein M. L., Chhiber R., 2018, *ApJ*, **865**, 25
- Velli M., 1993, *A&A*, **270**, 304
- Verdini A., Velli M., Buchlin E., 2009, *ApJ*, **700**, L39
- Verdini A., Velli M., Matthaeus W. H., Oughton S., Dmitruk P., 2010, *ApJ*, **708**, L116
- Verscharen D., Bale S. D., Velli M., 2021, *MNRAS*, **506**, 4993
- Wan M., Oughton S., Servidio S., Matthaeus W. H., 2012, *Journal of Fluid Mechanics*, **697**, 296
- Weber E. J., Davis Jr. L., 1967, *ApJ*, **148**, 217

- Wexler D. B., Stevens M. L., Case A. W., Song P., 2021, [ApJ](#), **919**, L33
- Wu P., Wan M., Matthaeus W. H., Shay M. A., Swisdak M., 2013, [Physical Review Letters](#), **111**, 121105
- Zank G. P., Matthaeus W. H., 1992, [J. Geophys. Res.](#), **97**, 17
- Zank G. P., Adhikari L., Hunana P., Tiwari S. K., Moore R., Shiota D., Bruno R., Telloni D., 2018, [ApJ](#), **854**, 32
- Zank G. P., Zhao L.-L., Adhikari L., Telloni D., Kasper J. C., Bale S. D., 2021, [Physics of Plasmas](#), **28**, 080501
- de Kármán T., Howarth L., 1938, [Proceedings of the Royal Society of London Series A](#), **164**, 192

This paper has been typeset from a $\text{\TeX}/\text{\LaTeX}$ file prepared by the author.